Real-Time Detection and Filtering of Radio Frequency Interference Onboard a Spaceborne Microwave Radiometer: The CubeRRT Mission

Joel T. Johnson ⓘ, Christopher Ball, Chi-Chih Chen ⓘ, Christa McKelvey, Graeme E. Smith ⓘ, Mark Andrews ⓘ, Andrew O'Brien, J. Landon Garry ⓘ, Sidharth Misra ⓘ, Rudi Bendig, Carl Felten ⓘ, Shannon Brown, Robert F. Jarnot, Jonathon Kocz, Kevin Horgan, Jared F. Lucey ⓘ, Joseph J. Knuble, Mike Solly, Carlos Duran-Aviles, Jinzheng Peng ⓘ, Damon Bradley, Jeffrey R. Piepmeier, *Senior Member, IEEE*, Doug Laczkowski, Matt Pallas, Nick Monahan, and Ervin Krauss

Abstract—The Cubesat radiometer radio frequency interference technology validation mission (CubeRRT) was developed to demonstrate real-time onboard detection and filtering of radio frequency interference (RFI) for wide bandwidth microwave radiometers. CubeRRT's key technology is its radiometer digital backend (RDB) that is capable of measuring an instantaneous bandwidth of 1 GHz and of filtering the input signal into an estimated total power with and without RFI contributions. CubeRRT's onboard RFI processing capability dramatically reduces the volume of data that must be downlinked to the ground and eliminates the need for ground-based RFI processing. RFI detection is performed by resolving the input bandwidth into 128 frequency subchannels, with the kurtosis of each subchannel and the variations in power across frequency used to detect nonthermal contributions. RFI filtering is performed by removing corrupted frequency subchannels prior to the computation of the total channel power. The 1 GHz bandwidth input signals processed by the RDB are obtained from the payload's antenna (ANT) and radiometer front end (RFE) subsystems that are capable of tuning across RF center frequencies from 6 to 40 GHz. The CubeRRT payload was installed into a 6U spacecraft bus provided by Blue Canyon Technologies that provides spacecraft power, communications, data management, and navigation functions. The design, development, integration and test, and on-orbit operations of CubeRRT are described in this article. The spacecraft was delivered on March 22nd, 2018 for launch to the International Space Station (ISS) on May 21st, 2018. Since its deployment from the ISS on July 13th, 2018, the CubeRRT RDB has completed more than 5000 h of operation successfully, validating its robustness as an RFI processor. Although CubeRRT's RFE subsystem ceased operating on September 8th, 2018, causing the RDB input thereafter to consist only of internally generated noise, CubeRRT's key RDB technology continues to operate without issue and has demonstrated its capabilities as a valuable subsystem for future radiometry missions.

Index Terms—Microwave radiometry, passive microwave remote sensing, radio frequency interference (RFI).

Joel T. Johnson, Christopher Ball, Chi-Chih Chen, Christa McKelvey, Mark Andrews, and Andrew O'Brien are with the Ohio State University, Columbus, OH USA (e-mail: johnson@ece.osu.edu; ball.51@osu.edu; chen.118@osu.edu; mckelvey.56@osu.edu; andrews.250@osu.edu; obrien.200@osu.edu).

Graeme E. Smith and J. Landon Garry are with the Johns Hopkins Applied Physics Laboratory, Laurel, MD USA (e-mail: smith.8347@osu.edu; garry.6@osu.edu).

Sidharth Misra, Rudi Bendig, Carl Felten, Shannon Brown, and Robert F. Jarnot are with the Jet Propulsion Laboratory, California Institute of Technology, Pasadena, CA USA (e-mail: sidharth.misra@jpl.nasa.gov; rudi.bendig@jpl.nasa.gov; carl.felten@jpl.nasa.gov; shannon.t.brown@jpl.nasa.gov; robert.f.jarnot@jpl.nasa.gov).

Jonathon Kocz is with the California Institute of Technology, Pasadena, CA USA (e-mail: jkocz@astro.caltech.edu).

Kevin Horgan, Jared F. Lucey, Joseph J. Knuble, Mike Solly, Carlos Duran-Aviles, Jinzheng Peng, Damon Bradley, and Jeffrey R. Piepmeier are with the NASA Goddard Space Flight Center, Greenbelt, MD USA (e-mail: kevin.horgan@nasa.gov; jared.f.lucey@nasa.gov; joseph.knuble@nasa.gov; michael.a.solly@nasa.gov; carlos.duran-aviles-1@nasa.gov; jinzheng.peng@nasa.gov; damon.c.bradley@nasa.gov; jeffrey.r.piepmeier@nasa.gov).

Doug Laczkowski, Matt Pallas, Nick Monahan, and Ervin Krauss are with the Blue Canyon Technologies, Boulder, CO USA (e-mail: dlaczkowski@bluecanyontech.com; matt.pallas@bluecanyontech.com; nmonahan@bulecanyontech.com; ekrauss@bluecanyontech.com).

Digital Object Identifier 10.1109/JSTARS.2020.2978016

I. INTRODUCTION

SATELLITE microwave radiometers have been providing measurements of key environmental variables since the late 1970s, including measurements of precipitation, water vapor, atmospheric and surface temperature, ocean salinity, cloud liquid water, sea ice, soil moisture, snow, and ocean winds. These systems face an ever increasing threat from man-made radio frequency interference (RFI) as the global wireless infrastructure has grown [1]–[10], putting at risk future radiometry missions. To mitigate this risk, future microwave radiometers will need to transition from the currently used analog systems to agile digital systems capable of extracting a clean geophysical signal even in bands polluted by RFI.

The Earth science microwave radiometry community has been working toward this goal for nearly two decades (see for example [11]–[16]) which led to the implementation of the successful radiometer digital backend technology currently operating in space in the Soil Moisture Active Passive (SMAP) mission [17], [18]. SMAP's RFI processing technology is limited to the narrow bandwidth (24 MHz) of the protected L-band spectrum used by SMAP, and requires a high data downlink rate, practically

eliminating it for consideration for higher frequency radiometer missions that use multiple channels each with bandwidths of several hundred MHz.

The recent emergence of fast sampling analog-to-digital converters (ADCs) and powerful field programmable gate arrays (FPGAs), along with the sustained advancement of processing algorithms used to remove man-made signals from the natural background, has now enabled wideband radiometer digital backends that can take RFI contaminated observations at input and produce an RFI-filtered integrated output signal onboard in real time. By performing RFI detection and filtering onboard and in real time, the requirement for high data rate downlinks is eliminated, making this technology feasible for use in all future radiometer missions. Real-time RFI mitigating digital backends have already been demonstrated in the laboratory and in airborne field campaigns [19]–[21].

The CubeSat Radiometer RFI Technology validation (CubeRRT) mission's purpose is to advance the readiness of this technology for future spaceborne missions by demonstrating successful real-time RFI filtering aboard a 6U CubeSat platform. CubeRRT was designed to demonstrate RFI processing over a broad set of frequencies that have been impacted by RFI covering commonly used bands for microwave radiometry in the 6–40 GHz range.

It is noted that the RFI processing performed by CubeRRT or any other RFI processing system cannot be completely effective in addressing RFI corruption, since portions of the measured time-frequency space must be discarded when performing a received power estimate. This results in a decreased radiometric resolution for the final measured brightness temperature, and no meaningful measurement is possible if the portion of time-frequency space observed is entirely corrupted by RFI. The possibility of low-level undetected RFI in the final brightness temperature product also remains. Therefore, while RFI processing technologies as demonstrated by CubeRRT are important tools to expand future radiometric measurements, the capabilities they enable do not reduce the need for regulatory protection of portions of the radio spectrum for radiometric observations.

Given that CubeRRT's design and prelaunch test results have been reported in part elsewhere [22]–[29], this article focuses on reporting multiple aspects of CubeRRT's final RFI algorithms that have not been previously described (in particular the three levels of "flattening" used in CubeRRT's cross-frequency detection), as well as on-orbit results. A brief review of the instrument design and prelaunch test results is also provided as context for these discussions. Accordingly, Section II provides an overview of CubeRRT payload design considerations, and Section III then reviews the radiometer digital backend (RDB) and radiometer front end (RFE) subsystems. Section IV describes CubeRRT operations, datasets, and prelaunch tests, while Section V focuses on postlaunch measurements, and Section VI provides final conclusions. A detailed description of CubeRRT's antenna subsystem is provided in [29].

II. CubeRRT Payload Design Considerations

The CubeRRT mission was designed to address several challenges associated with demonstrating microwave radiometer

TABLE I
SUMMARY OF CUBERRT DESIGN GOALS.

Frequency	6 to 40 GHz Tunable, 1 GHz instantaneous
Polarization	Circular polarization
Observation angle/Orbit (ISS launch)	0° Earth Incidence Angle 400 km altitude, 51.6° orbit inclination
Spatial Resolution	80 km (40 GHz) to 240 km (6 GHz)
Integration time	100 msec
Ant Gain/ Beamwidth	12dBi/30° (6 GHz), 21 dBi/10° (40 GHz)
Interference Mitigation	On-board Nyquist sampling of 1 GHz spectrum; On-board real-time Kurtosis and Cross-Frequency Detection Downlink of frequency resolved power and kurtosis in 128 channels to verify on-board performance
Calibration	Internal: Reference load and Noise diode sources External: Cold sky and Ocean measurements

technologies in the 6–40 GHz range from a CubeSat platform. First, typical microwave radiometer science instruments operating at frequencies in the 6–40 GHz range use antenna apertures of 1 m or more in diameter to achieve spatial resolutions on the order of 10–60 km. Because of size limitations imposed by its 6U form factor, CubeRRT's technology validation goals were specific to RFI detection and filtering, driving more modest spatial resolution requirements. Any RFI sources within CubeRRT's antenna pattern will be captured and observed, and filtering of these sources, regardless of the spatial resolution of the background scene or the type of RFI source, serves to validate the RFI processing technology. CubeRRT was therefore planned with an antenna subsystem compatible with CubeSat operation. It is noted that the strength of an observed RFI source follows the "density of interferers" equation [5], which states that the RFI-induced brightness temperature in Kelvin is proportional to the total effective isotropic radiated power (EIRP) per unit area within the radiometer's footprint. CubeRRT's larger footprint of 80 km (40 GHz) to 240 km (6 GHz) diameter then makes a single point RFI source appear weaker in terms of brightness temperature. However, the high sensitivity of the CubeRRT digital backend enables many RFI source types of even $<\sim$2 K to be detected and mitigated, so that high sensitivity RFI measurements nevertheless can be achieved.

Table I summarizes CubeRRT observation properties specified in the design process. CubeRRT observes Earth emissions at 0 degrees Earth incidence angle (to improve spatial resolution) in a single circular polarization and at 100 ms reporting interval. Although CubeRRT was designed to output both the "original" and "clean" uncalibrated total powers corresponding to 100 ms integration over the full 1 GHz bandwidth, CubeRRT is also capable of reporting measured powers and the associated kurtosis values in 128 frequency channels within the 1 GHz bandwidth. This finer resolution "spectrum" data allows the performance of the onboard processor to be validated in ground processing, thereby providing a complete assessment of onboard performance as a function of RFI source type, frequency content, and power levels.

The data capacity of up- and down-link communications was also an important consideration in the design process and in payload operations planning, particularly given the maximum 3 Mb/s downlink data transfer rate available from the spacecraft UHF Cadet radio. CubeRRT's ground communications are supported by the NASA Wallops Flight Facility ground station, with an availability of one 6 min contact per day (on average). Due to the need to retain flexibility in the payload data rate, CubeRRT was designed with a variety of data packet types, including those that reported the full 128 frequency channel power and kurtosis values ("full-spectrum" data packets) as well as those that reported only the integrated channel powers before and after RFI filtering ("no spectrum" packets).

The wide bandwidth requirements on the RFE (6–40 GHz) as well as the significant processing requirement of a 1 GHz bandwidth signal result in a power consumption of approximately 30 W for the entire payload. Power dissipation was therefore originally assessed as the "tightest" requirement for CubeRRT operations. Preliminary power analyses showed that 20% orbital averaged energy margin would be available provided that CubeRRT operated at a 25% duty cycle (i.e., payload operates 25% of the time on average). This conservative estimate was later extended to an expected 33% duty cycle of operation, and later project activities achieved 75–100% duty cycle of payload operations as will be described in Section V.

CubeRRT's RFE, RDB, and ANT subsystems were designed to be compatible with deployment on a 6U CubeSat bus developed by Blue Canyon Technologies (BCT). The spacecraft includes the BCT XB1 high performance spacecraft system with the majority of the spacecraft structure available for the payload. The BCT XB1 spacecraft system provides power, attitude control, command and data handling (C&DH), and payload interface subsystems.

III. PAYLOAD RDB AND RFE SUBSYSTEMS

A. Radiometer Digital Backend

CubeRRT's RDB is the key mission technology and is responsible for the following functions.

1) Sampling the 1 GHz bandwidth signal provided by the RFE.
2) Performing real-time RFI processing of the sampled signal.
3) Outputting the observed total power before and after RFI filtering at a nominal 10 Hz rate.
4) Outputting the power and kurtosis observed in 128 frequency subchannels at a nominal 10 Hz rate.
5) Applying an optional lossy compression algorithm to the output data to meet output data rate requirements.
6) Accepting and responding to commands from the spacecraft.
7) Implementing a 16 state CubeRRT calibration sequence and a controllable tuning sequence.
8) Controlling RFE settings as part of the calibration and tuning sequences.
9) Sending payload output data as well as RFE and RDB health telemetry to the spacecraft computer.

The CubeRRT RDB achieves these functions with a maximum power dissipation of 10 W, a 170 g mass, an A/D converter sampling rate of 2 GSPS, and 8 b precision per A/D sample. The RDB design is similar to that described in [20], to which the reader is referred for additional details. Photographs of the implemented RDB are available in [25].

Both kurtosis and cross-frequency RFI detection algorithms are implemented by the RDB. The former is a more general RFI detection method that has been shown to be effective particularly for short pulsed interference (i.e., interference pulses that occupy only a small fraction of the 100 ms integration period) while the latter is highly effective for more continuous RFI types [12]–[15]. Analyses performed in the system design study showed that the combination of these algorithms is capable of meeting CubeRRT's RFI detection goals [20]. Fig. 1 summarizes the basic firmware processing operations of the RDB, including the creation of 128 frequency subchannels, the computation of the second and fourth moments of the complex signal in each frequency subchannel, and the integration of these products resulting in their final reporting at 100 ms time resolution. RFI detection is performed on the accumulated 100 ms products and can be performed either in firmware (implemented in FPGA hardware) or in software (run on the processor embedded within the FGPA).

In what follows, the complex amplitude in subchannel k (of 128 subchannels, $k = 0$ to 127) in the lth time interval can be written as

$$Z_{k,l} = X_{k,l} + iY_{k,l} \tag{1}$$

from which the signal second moment is obtained as

$$M_{k,2} = \frac{1}{L} \sum_{l=1}^{L} \left(X_{k,l}^2 + Y_{k,l}^2 \right) \tag{2}$$

and the fourth moment as

$$M_{k,4} = \frac{1}{L} \sum_{l=1}^{L} \left(X_{k,l}^4 + Y_{k,l}^4 \right). \tag{3}$$

Note one sample of $Z_{k,l}$ is obtained every 128 ns given the 2 GSPS sample rate. In addition, $M_{k,4}$ is computed by summing $X_{k,l}^4 + Y_{k,l}^4$, rather than $(X_{k,l}^2 + Y_{k,l}^2)^2$ because the kurtosis values computed using these two quantities in the absence of interference have similar statistical properties after a multiplicative scaling.

A key goal for the CubeRRT project is the validation of the RFI flags created onboard the spacecraft through comparison with RFI flags generated by ground processing using the measured spectra. Accordingly, the RDB can be commanded so that its outputs include the reporting of $M_{k,2}$ and $M_{k,4}$ ("full-spectrum" data packets), exclude these quantities ("no spectrum" data packets), or include a compressed version of these quantities ("compressed spectrum" packets), as discussed in what follows. Validation of onboard generated flags is fully possible only in the specific case that all "full-spectrum" data is downlinked, because only in this situation is the information available on the ground identical to that on the spacecraft. Because compressed spectrum
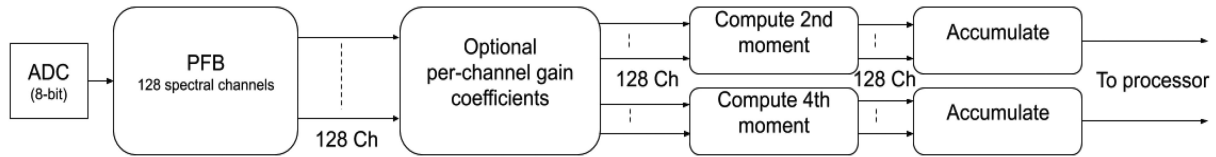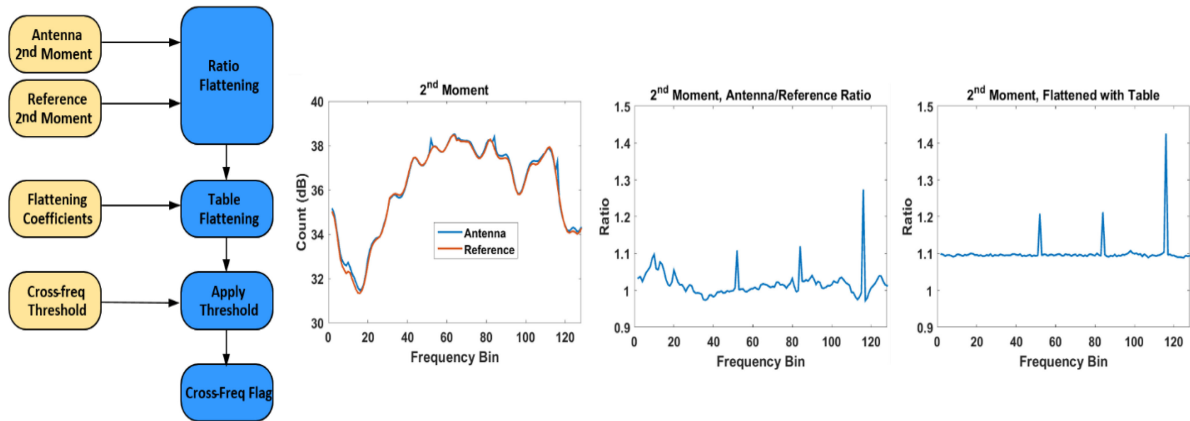
Fig. 1. Schematic of RDB firmware operations.

Fig. 2. (Left) Overview of cross-frequency algorithm. (Right) Sequence of plots illustrating original second moment versus frequency (including Level 1 flattening only), antenna over reference spectrum (Level 1 and Level 3 flattening applied), and "flattened" antenna over reference spectrum (Level 1, 2, and 3 flattening applied).

data often provide a good approximation of the onboard information (as described subsequently), assessments using compressed data can also be used for validation, although tests showed that a deviation of the flags reported in ∼1% of the flags computed. Ground validation is not possible for "no spectrum" packets because no spectrum information is available.

Kurtosis Algorithm: Implementation of the kurtosis detection in each frequency subchannel follows the process described in [20], in which the fourth moment is compared to a threshold multiplied by the second moment squared so that no division processes are required in firmware. Thresholds are set according to the methods described in [20].

Both the second and fourth moments are resolved as 64 b quantities onboard the RDB's FPGA so that highly accurate detection flags (and kurtosis values if desired) are available. However, the need to reduce the data size of the output "spectrum" products required that the second and fourth moments be reported in only 16 b resolution. Because of this, a commendable "shift" value (called "M2_shift" and "M4_shift"), respectively, is used to select the 16-b window to be output within the 64-b products. Ideally, these values are chosen so that the full 16-bit precision is retained in output products over a wide dynamic range. However large variations in the input power can result in non-optimal M2_shift or M4_shift settings causing a reduction in the output precision to a smaller number of bits. This is an issue particularly for the fourth moment, due to the high dynamic range of this quantity. Note that these settings affect only the output moment products that are used for performance validation, because the full 64-bit onboard precision is used in generating the real time kurtosis flag. However, attempts to reproduce the onboard generated flags for validation using the downlinked

moments can be impacted if the dynamic range is reduced by nonoptimal selection of the 16-bits from the original 64-bit values. Prelaunch testing was performed to select these values to avoid significant impacts on the output product precision. An alternate "compressed" packet format was also developed to avoid these issues by reporting the kurtosis computed onboard prior to reduction to 16 b as an index to a 256-point lookup table of kurtosis values; the lookup table was defined to have a fine resolution in the kurtosis (smaller than the nominal standard deviation) near the nominal value of 3, and a coarser resolution for larger deviations from 3. This approach was found to be desirable in optimizing the output data product size because kurtosis is the quantity of primary interest for RFI flagging, not the fourth moment.

Cross-Frequency Algorithm: Fig. 2 illustrates the cross-frequency RFI detection algorithm [14], [15], which flags "outliers" in the power versus frequency for a single 100 ms second moment spectrum. The cross-frequency algorithm assumes that thermal noise should have a spectrum that is "flat" in frequency; any subchannel second moment (i.e., power) values that are significantly different from the other subchannels should therefore be flagged. The algorithm proceeds for a given input spectrum by computing the median second moment of the input 128 moments $(M_{\mathrm{med},2})$ and flagging any subchannels satisfying

$$M_{k,2} > M_{\mathrm{med},2}\left(1 + \frac{T_{\mathrm{cross}}}{\sqrt{L}}\right) \tag{4}$$

with T_{cross} a selectable threshold used to set the false alarm rate. The inclusion of $\sqrt{L}$ in (4) provides an approximate correction for changes in L but has no significant impact because L is fixed for CubeRRT operations (to correspond to a 100 ms integration

period) and because T_{cross} can be varied as needed to control detector performance. For CubeRRT, T_{cross} is a single value that is set independently of RFE tuning.

A key challenge for the cross-frequency algorithm is the fact that it operates on data that has not been calibrated, so that spectral "flatness" is not assured (e.g., see the second plot of Fig. 2). Avoiding the flagging of second moment variations in frequency can be achieved by increasing T_{cross}, but the excessively high T_{cross} values that result can compromise detection sensitivity. CubeRRT's RFI processor addresses this challenge by implementing three types of spectrum "flattening" operations. The first, labeled "Level 1" flattening, multiplies all measured spectra by a static table of 128 64-bit coefficients prior to any subsequent operations, including the reporting of the final output second-and fourth-moment products. The coefficients used are intended to compensate the passband response of the RDB A/D converter and other electronics, which are common to all CubeRRT measurements; Level 1 flattening is always "turned ON" due to this fact. Level 1 flattening is desirable because CubeRRT's 1 GHz bandwidth input signal is centered in the first alias region of the digitizer (1–2 GHz IF, sampled at 2 GSPS), and the RF gain of the ADC decreases in frequency. Level 1 flattening coefficients are stored in the RDB and can be modified by command (and if set to unity would result in "turning OFF" Level 1 flattening).

"Level 2" flattening is implemented similarly to Level 1 flattening in that the measured spectrum is again multiplied by an additional set of 128 coefficients, in this case resolved at 32 b each. The coefficients used for Level 2 flattening, however, are selected from a larger table of 4480 coefficients based on the current radiometer tuning frequency so that variations in the RFE response versus frequency can be compensated. Level 2 flattening values are determined through prelaunch measurements of instrument passband shape during tuning of the center frequency from 6 to 40 GHz.

Although the RFE is capable of tuning over a wide range of center frequencies, limitations in the RDB onboard memory allowed only a 4480 point table to be created, representing a maximum of 35 sets of "full channel" 128 point values over the full 34 GHz tuning range. The mapping between the RFE tuning frequency and the table index also is performed using a simple linear scaling algorithm in order to simplify operations. This implies that an RFE tuning frequency having a portion of its bandwidth overlapped with a portion of the bandwidth at another nearby RFE tuning frequency may not be optimally flattened, since the coefficients in the Level 2 table must be selected for a specific frequency using only one RFE tuning frequency.

Level 2 flattening coefficients also can be updated by spacecraft command, but the larger size of the table results in a large number of commands required to update the entire table. Level 2 flattening differs from Level 1 flattening in that it is applied only to antenna measurements (and not to internal calibration load measurements), it is used only in generating cross-frequency flags and does not modify the output second and fourth moments, and it can be selected to be "ON" or "OFF" by command.

While Level 2 flattening alone can be used to reduce spectrum variations and improve the sensitivity of the cross-frequency algorithm, any variations in the system passband response at any
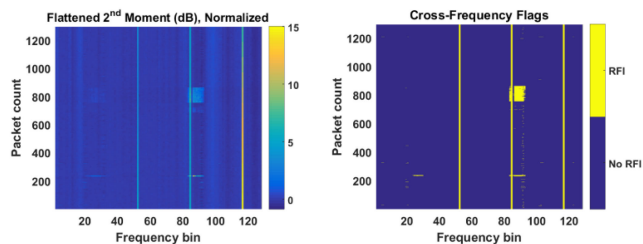

Fig. 3.   (Left) Example input flattened second moment spectra. (Right) Flags produced by the cross-frequency algorithm.

frequency with temperature or other system properties would again result in larger spectral variations causing either increased false alarms or a requirement to reduce detection sensitivity by increasing T_{cross}. The implementation of a flattening approach that calibrates any dynamic system response variations is therefore desirable. One method for achieving dynamic flattening (as used by the SMAP RFI processing algorithm) involves performing a complete calibration of the second moment spectrum before applying the cross-frequency algorithm to the calibrated spectrum. While onboard calibration is feasible given that the RDB controls the radiometer calibration switching cycle and therefore has knowledge of measurements in all calibration states, using this method would place greater requirements on RDB onboard data storage and processing. Knowledge of the instrument postlaunch calibration would also be required. This knowledge would likely not be available until instrument commissioning activities were completed.

A simpler approach was therefore pursued as the "Level 3" flattening method. In this method a "quasi-calibration" is performed that uses measurements of the radiometer reference load. Level 3 flattening is implemented by dividing the observed antenna spectrum by the average of all spectra of reference load measurements within the same calibration cycle (see Section IV for additional information on the CubeRRT calibration cycle). In this manner, the spectrum input to the cross-frequency algorithm is the "antenna over reference" spectrum in which any passband variations common to both the antenna and reference measurements are compensated (see example in Fig. 2). Because the division of the noise-containing antenna and reference measurements results in a quotient with increased noise, the reference spectrum is first averaged before the ratio is computed. As with Level 2 flattening, Level 3 flattening is by definition applied only to antenna measurements. Also it is used only in generating cross-frequency flags and does not modify the output second and fourth moments, and can be selected to be "ON" or "OFF" by command.

While the Level 3 flattening method should largely cancel passband variations internal to the CubeRRT radiometer, it does not compensate any passband variations outside the reference load calibration loop. However, by combining both Level 2 and Level 3 flattening, with the Level 2 table defined to compensate these responses, a final spectrum having greatly increased "flatness" can be input to the cross-frequency algorithm (right most plot of Fig. 2).

Fig. 3 illustrates an example time series of second moment spectra after the application of Level 1, 2, and 3 flattening, and
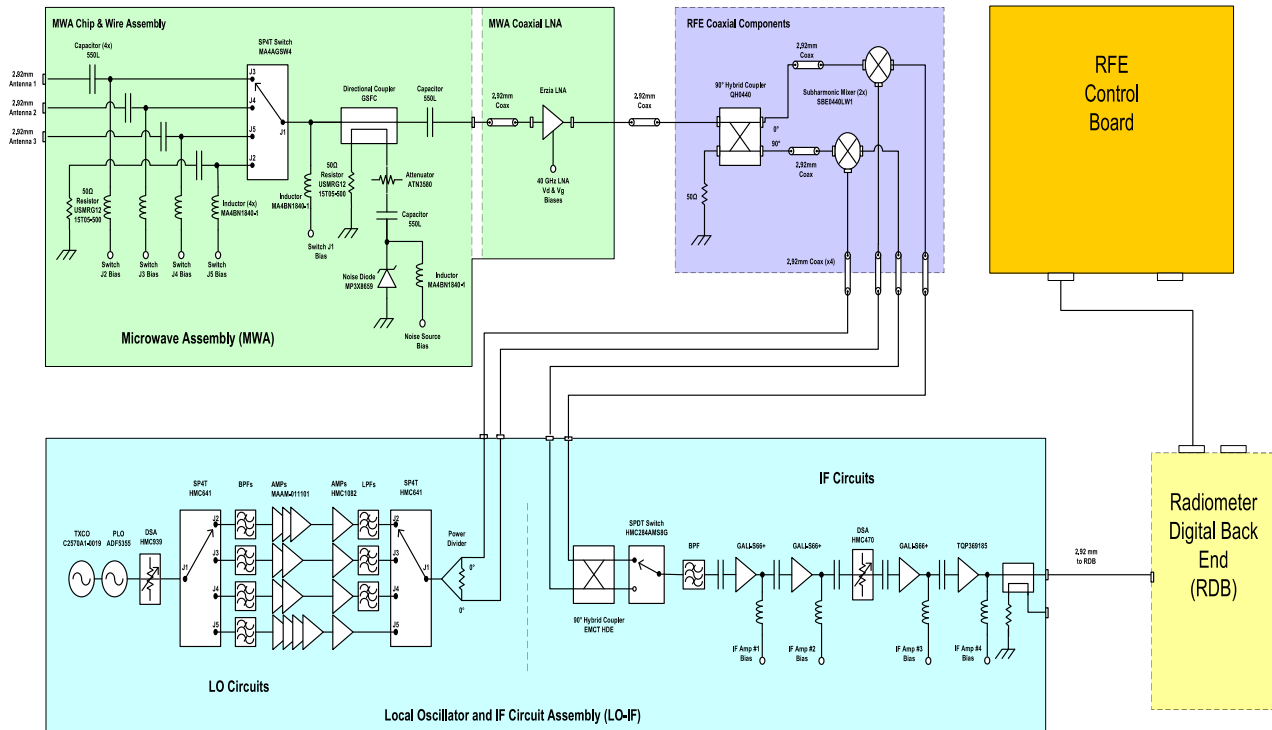
Fig. 4.   Overview schematic of CubeRRT's RFE.

the associated cross-frequency algorithm flags reported showing good detection performance with minimal false alarms. It is noted that even after the application of flattening at Levels 1, 2, and 3, some residual variations in measured spectra can remain in the absence of RFI due to changes with temperature. These variations can require T_{cross} to be increased (with a corresponding reduction in detector sensitivity) to avoid an excessive false alarm rate. To address this concern, variations in the system passband response with temperature were recorded in prelaunch testing (see Section IV-C), and multiple sets of Level 2 coefficients were recorded that correspond to these temperatures. To avoid the need to upload these coefficient tables from the ground postlaunch, scripts were placed onboard the spacecraft prior to launch that contained the commands necessary to implement one of four Level 2 coefficient tables (~ -10, 5, 20, and 40 °C estimated temperatures) through a single spacecraft command.

B. Radiometer Front End

CubeRRT's radiometer front end (RFE) subsystem receives incoming RF signals from the three payload antennas [29], and selects one of these signals for amplification, downconversion, and filtering to the 1–2 GHz IF range sampled by the RDB. The 1 GHz IF signal provided can be tuned over the range 6–40 GHz through this process, and the RFE also provides additional reference load and reference plus noise diode states for internal radiometric calibration. Telemetry on RFE temperatures, voltages, and currents is also provided to the RDB through a voltage-to-frequency telemetry conversion system. The wide bandwidth capabilities of the RFE stand in contrast to traditional radiometers, which typically implement independent RF front ends for individual narrowband RF channels. The RFE's wide bandwidth made the development of the RFE challenging, particularly with regard to the goal of ensuring acceptable sensitivity and stability over the entire tuning range. The requirement to operate within CubeRRT's mass, volume, and power limitations of 2.8 kg, $\sim$1.1 U, and 11 W, respectively, further represented a significant challenge for RFE development.

It is noted that CubeRRT's goal of validating onboard RFI processing does not necessarily require that science-quality radiometer radiometric resolution (typically specified as a radiometer noise-equivalent delta temperature (NEDT) of 1 K or better) be achieved, since onboard detection and filtering can be performed using RFI amplitudes greater than this level. Because of this fact, CubeRRT's RFI detections are assessed as detections at the level of twice the radiometer NEDT, whatever that NEDT may be in a given portion of CubeRRT's frequency range. Nevertheless, the CubeRRT project strived to attain a radiometric resolution representative of science-quality measurements in at least some portion of the tuning range, and within an order of magnitude of science-quality performance across the entire tuning range.

Fig. 4 provides an overview schematic of the RFE illustrating its basic functionality. The three CubeRRT payload antennas provide signals in the bands 6–11, 11–22, and 22–40 GHz, respectively, and the input four-port switch allows for selection of one of these bands or a reference load termination. A coupler for injection of the noise diode calibration source is then followed by amplification and a quadrature downconversion that is used to provide IF outputs representing either the upper or lower sidebands occupying 1–2 GHz above or below the local oscillator frequency. A final IF stage provides an additional

Fig. 5. Estimated CubeRRT radiometric resolution versus frequency obtained from RFE/RDB prelaunch tests.

Fig. 6. Baseline CubeRRT calibration cycle.

controllable gain (through a controllable step attenuator) and an IF band definition filter.

Generation of the required 8–38 GHz local oscillator (LO) is accomplished through a "switched bank" configuration in which either the zeroth, first, second, or third harmonics of an original 8–14 GHz oscillator are selected depending on the desired band. Due to the differing gains of each of these configurations, each of the individual banks has a differing additional gain included, along with an LO filter to eliminate other harmonics in the output signal. A programmable attenuator is also used to control the output LO power further and to achieve an LO power level input to the mixer of ∼10 dBm.

Control of the RFE includes the specification of the antenna switch port selected, the noise diode ON/OFF state, the LO bank selection, and the LO and output IF programmable attenuator settings. Values for these parameters are provided by the RDB as part of the CubeRRT frequency tuning sequence. The required values were determined in prelaunch testing and are stored in a table onboard the RDB. The RFE also reports 16 telemetry states obtained from multiple thermistor measurements (for temperatures), voltage measurements of in-line series resistors on the input +7.5 and +15 V power supplies, and direct voltage measurements of these supplies. The temperature values obtained from the thermistors (particularly of the "reference load" on the input switch) are used in radiometer calibration.

Radiometric performance testing resulted in the estimated NEDT levels versus center frequency reported in Fig. 5. These results were obtained through examination of the standard deviation of cryotarget measurements over a long time series following the application of a high pass filter to eliminate slow changes in target brightness temperatures. The results show 100 ms NEDT values ranging from as low as 0.4 K at frequencies less than 10 GHz up to ∼5 K from 30–35 GHz and <10 K up to 37 GHz. Results for both the upper and lower sidebands are included in the plot; in cases where both are available, the sideband providing the lowest NEDT value was selected for operational use. These values are sufficient throughout the 6–37 GHz range to provide RFI detections (at the 2 NEDT level) that are relevant for science applications, particularly at frequencies less than ∼30 GHz. Note that without an RFI detection subsystem, even a 20 K RFI contribution can be difficult to detect in many situations because geophysical scenes can often

show brightness variability in the 20–50 K range. Photographs of the implemented RFE are available in [26] and [27].

IV. CubeRRT Payload Operations, Data Products, and Prelaunch Tests

A. Payload Operations

CubeRRT's goal of demonstrating onboard detection and filtering of RFI emphasizes measurements in ten frequency bands commonly used for microwave radiometry (centered at 6.8, 10.4, 18.7, 19.4, 22.2, 23.8, 31.4, 34, 36.5, and 37.5 GHz, respectively); these bands are referred to as the ten "golden frequencies" in what follows. While CubeRRT is capable of tuning to a wide range of frequencies within the 6–40 GHz range, the emphasis on the golden frequencies resulted in an initial operational focus on these frequencies with the possibility of later mission measurements expanding to other bands. CubeRRT's antenna footprint of ∼40 to 240 km on the Earth's surface combined with an orbital velocity of ∼6 km/s shows that a minimum of 6.7 and a maximum of 40 s are available to observe each antenna footprint. CubeRRT's 10 Hz data reporting rate then results in 67 to 400 records per antenna footprint. It is also noted that measurements of the reference load and reference plus noise diode states are required periodically for radiometer calibration. Also, it is desirable to be able to specify the type of measurement packet (i.e., "full spectrum", "no spectrum", or "compressed spectrum") for each step in the calibration sequence in order to have flexible control of the payload data rate.

Given the variety of combinations of tuning frequencies and calibration states that can be envisioned in this situation, CubeRRT's payload commanding was developed to maximize flexibility. The primary payload command is denoted "RDB_MEASURE" and specifies an "inner loop" over a 16 state calibration and packet type sequence, followed by an "outer loop" over a set of tuning frequencies (which can range from 1 to a maximum of 10 in a single command), followed by a "final loop" that repeats the entire pattern a specified number of times. Fig. 6 illustrates the default CubeRRT calibration and packet type sequence, which includes one "noise diode plus reference state", three "reference" states, and 12 "antenna" states. One compressed spectrum packet is recorded for the former two states, and two for the antenna states, while the remaining states are "no spectrum" (denoted L in Fig. 6) packets. This calibration sequence was found acceptable for system calibration in prelaunch tests.

CubeRRT's default mode of operation (i.e., if no command is provided by the RDB) uses this sequence, looping through the ten "golden" frequencies and repeating the calibration sequence nine times for each golden frequency (i.e., a total of $16 \times 9 = 144$ measurements representing 14.4 s at each frequency before tuning into the next frequency). This default mode of

operation was selected to provide an approximate minimum of one frequency per footprint at the highest CubeRRT frequencies while providing multiple observations per frequency per footprint at the lower CubeRRT frequencies. The flexibility of the RDB_MEASURE command enables a variety of other observation strategies, including extended dwells at a single frequency, increases or decreases in the amount of moment data reported, and changes in the calibration cycle. Other payload commands include an "RDB_SPECTROMETER_SET" command for setting detection thresholds and configuring the spectrometer and RFE IF attenuator, an "RDB_ADC" command for acquiring a "snapshot" the A/D converter samples without further processing (for system testing), and "RDB_TABLE_SET" command for modifying the Level 1 and Level 2 flattening coefficients discussed in Section III-A.

B. CubeRRT Data Products

Payload data received from the spacecraft is uploaded daily to a file server as one binary payload data file containing payload packets and as a spreadsheet containing time stamped bus navigation and attitude information as well as selected bus voltages, currents, and temperatures. The daily data volume acquired by CubeRRT in the baseline mode is ∼29 MB at a duty cycle of 25%. Other operational modes of interest include 75% or 100% duty cycle operations in 100% "no spectrum" data, which represent ∼38 and 50 MB/day, respectively.

Level 0 CubeRRT data from the spacecraft is processed into a L1A data product in HDF5 format. In addition to format conversion, the L1A processor translates payload housekeeping telemetry data into engineering units using appropriate calibration processes for these quantities. L1A CubeRRT files can then be further processed into L1B files that contain geolocated calibrated brightness temperatures and ground-reproduction of the onboard RFI flagging process, all reported for each CubeRRT data packet. Calibration is performed using a standard radiometer internal calibration, based on knowledge of the reference load physical temperature (from RFE thermistor measurements) as well as the excess brightness contributed by the noise diode as a function of frequency (determined through prelaunch testing). External calibration is performed through a correction for the antenna loss as a function of frequency. Calibration is also performed both for the radiometer total channel power and mitigated powers, as well as for the 128 point spectrum. Recall that Level 2 and Level 3 flattening is used only in the determination of RFI flags and does not affect the output second moment data used to produce calibrated brightness temperatures. Because CubeRRT data can be calibrated both before and after RFI flagging, it is possible to determine the RFI level observed in Kelvin as the difference of these two quantities.

As discussed previously, a key goal is the validation of the RFI flags created onboard the spacecraft through comparison with RFI flags generated in ground processing. A complete validation is possible only when the instrument provides "full spectrum" packets. It is also noted that the use of Level 3 flattening results in antenna measurements being normalized by the average of all reference state measurements within a calibration cycle prior to the generation of the cross-frequency flag. If spectrum data are

not available for all reference states, the quality of flag reproduction may also be impacted, at a level of up to 1%. In these situations, a reproduction of flags to within the 1% level (i.e., 99% of flags are generated identically and 1% differ) represents an acceptable validation. The reproduction of flags on the ground follows the algorithms described in Section II, and requires knowledge of any Level 2 flattening table used onboard the spacecraft.

CubeRRT's ultimate goal is the production of a calibrated full bandwidth brightness temperature that has RFI contributions automatically removed. Because calibration is not performed onboard the spacecraft, the reported "unmitigated total power" and "mitigated total power" may represent differing portions of CubeRRT's passband, which requires correction as part of onground calibration processing. This correction is implemented as follows.

1) Given the second moment power, $M_{k,2}$, in each frequency bin $k = 0$ to 127, the "unmitigated total power" is $P_u = \sum_{k=1}^{127} M_{k,2}$; note the bin $k = 0$ is excluded as it is the "dc" bin corrupted by any dc biases.

2) The RFI flagging process results in the "mitigated" power being a similar sum over a set of "clean" indices, $P_m = \sum_{k=\bar{k}_c} M_{k,2}$. The set of flagged indices is denoted as $\bar{k}_f$.

3) We desire to estimate $P_{m,\text{corr}}$ which should approximate P_u with RFI contributions excluded.

4) For each RF center frequency, we assume prior knowledge of the fractional contribution of each bin to the total power in situations without RFI, i.e., $f_k = \frac{\langle M_{k,2} \rangle}{\sum_{k=1}^{127} \langle M_{k,2} \rangle}$, with the $<>$ notation indicating an average over RFI free situations. Knowledge of f_k may be obtained from prelaunch testing or from a long term average over postlaunch measurements expected to be RFI free.

5) The corrected "mitigated" power is then $P_{m,\text{corr}} = \frac{P_m}{1 - \sum_{k=\bar{k}_f} f_k}$; this power is then used to produce the calibrated mitigated brightness temperature.

The L1B processor implements this correction and produces an HDF formatted output file containing geolocated calibrated brightness temperatures and reproduced RFI flags. Reproduced RFI flags are reported for the kurtosis and cross frequency algorithms, as well as the combination of flags used for a particular packet. Note that downlinking information on the onboard flag status (1 bit for each of the 128 subchannels) is required in this process so that $P_{m,\text{corr}}$ can be computed on the ground.

C. Prelaunch Tests

Prelaunch tests of the CubeRRT payload and fully integrated spacecraft are described in part in [26] and [27]. Payload testing included radiometric characterization (as in Fig. 5) as well as RFI performance tests (see [26] and [27]). The entire integrated spacecraft was operated through 104 h in a thermal vacuum chamber within which conditions were representative of those to be encountered on orbit. No issues were encountered during this period, and the testing provided the opportunity to characterize the sensitivity of the Level 2 flattening table to changes in temperature. Fig. 7 provides an example of these results in which relative variations in the antenna over reference spectrum are shown as a function of the reference load
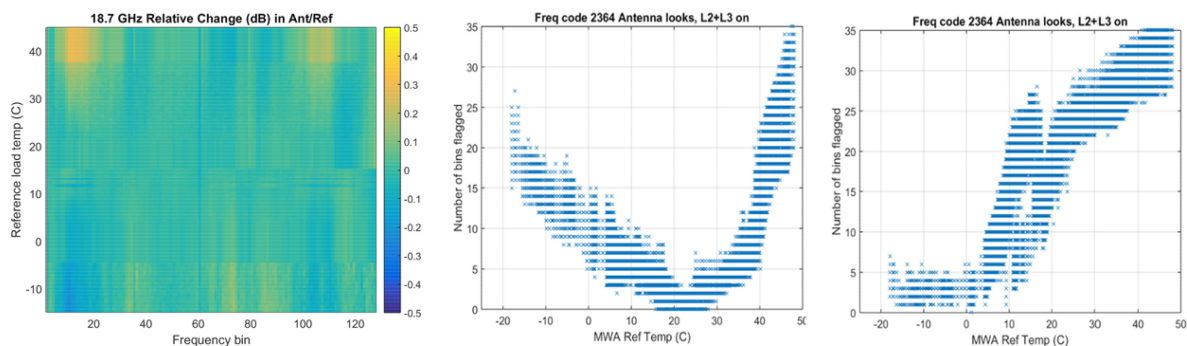
Fig. 7. Examples illustrating CubeRRT power variations with temperature: (Left) 18.7 GHz channel relative change in antenna/reference load power in dB. (Middle) On-board flagging of 18.7 GHz channel using a flattening table developed for 20 °C. (Right) Flagging of 18.7 GHz channel using flattening table developed for −10 °C.
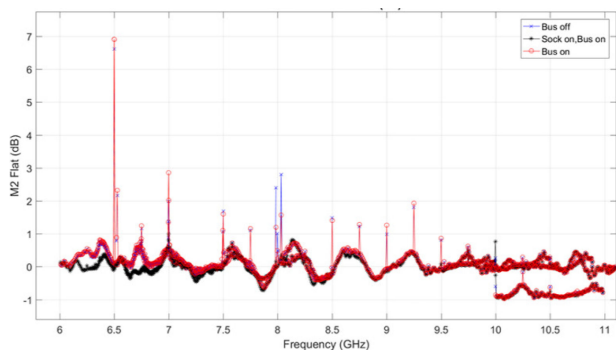

Fig. 8. CubeRRT average antenna over reference spectrum measured in prelaunch self-compatibility testing showing presence of 250 MHz clock harmonics.

physical temperature (which varied significantly through the thermal cycle). The results show changes in the reference spectrum to be modest (i.e., within +/−0.5 dB) so that frequent updates to the onboard Level 2 flattening table should not be required. The middle and right plots of Fig. 7, however, do demonstrate the sensitivity of the cross frequency algorithm to temperature. These plots illustrate the number of cross-frequency flags obtained per spectrum on average as a function of reference load temperature when a given Level 2 flattening table is used (20 °C table for the middle plot, and −10 °C table for the right plot). While variations in temperature up to ~±10 °C result in only modest increases in flagging, larger variations could cause more significant changes, motivating the inclusion of multiple Level 2 coefficient tables aboard the spacecraft.

Prelaunch self-compatibility testing of the integrated spacecraft also identified a source of self-interference caused by the RDB subsystem. Testing showed that harmonics of an RDB 250 MHz clock were received by the CubeRRT antenna even at frequencies as high as 11 GHz. Fig. 8 illustrates these effects as recorded during payload self-compatibility tests in an anechoic chamber for multiple payload configurations. The "spikes" observed every 250 MHz in the antenna over reference spectrum shown are caused by self-interference. The spectra shown in Fig. 8 are combined over multiple tuning frequencies in order to obtain the 6–11 GHz plot illustrated. The multiple traces shown from 10–11 GHz arise due to the use of the upper or lower side-bands in this case.

Following the test, possible mechanisms for the reception of 250 MHz clock harmonics and any options for remediation (for example, by installing additional RF absorbing or shielding materials within the payload volume) were investigated. However, it was determined that any such modifications would result in unacceptable schedule delays. The project also performed analyses of the impact of the self-generated emissions on CubeRRT measurements. Because CubeRRT packets can resolve the measured spectrum, it is possible when spectrum data are available to identify the 250 MHz harmonics and to quantify their impact in postprocessing. Also, because the self-generated RFI remains constant in time, it represents a fixed RFI bias that can be accounted for and compensated when analyzing the results obtained. Therefore the project determined to proceed without further action.

Test results were also used to update the Level 2 flattening coefficient tables to account for the impact of the payload antenna on the passband response. Two options were available regarding the 250 MHz self-generated RFI contributions. The first would include the 250 MHz spurs in the definition of the flattening table, so that these spurs would be considered "nominal" and would not be detected as RFI. The second option would not include the spurs in the flattening table (and would reproduce the necessary coefficient values by interpolation over points not containing spurs), so that the spurs would remain "anomalous" and would be flagged as RFI. Because the self-generated RFI signals do not represent external noise contributions and should be excluded from the "RFI-free" output, the second approach was implemented. This selection results in a maximum of 4 channels out of the 128-channel spectrum being flagged as corrupted by the self-generated spurs. One outcome of this process is that CubeRRT measurements inherently contain the "test" RFI signals of the 250 MHz harmonics, thereby providing a continuous opportunity to assess RFI algorithm detection performance. This opportunity subsequently proved valuable in analyzing CubeRRT RFI processor outputs.

Following the completion of all prelaunch tests, the CubeRRT spacecraft was transported to Houston, TX, USA, on March 21st, 2018, for integration into the Nanoracks deployment module [30], [31]. CubeRRT was integrated into a deployment module along with the TEMPEST-D 6U spacecraft, oriented such that TEMPEST-D would emerge prior to CubeRRT upon deployment from ISS. Fig. 9 shows a photograph of the CubeRRT
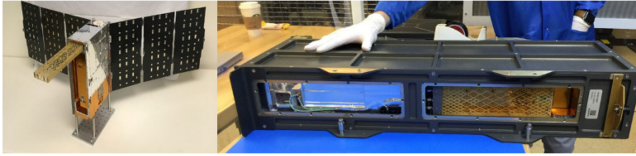
Fig. 9. (Left) Photograph of CubeRRT spacecraft (on mounting platform) prior to delivery to Nanoracks. (Right) Photograph of CubeRRT spacecraft integrated into Nanoracks deployment module along with the TEMPEST-D spacecraft.

spacecraft prior to delivery (left) along with the spacecraft integrated with TEMPEST-D into the Nanoracks deployment module (right). Nanoracks subsequently performed further acceptance testing and delivered the spacecraft for continued integration part of the OA-9 Cygnus spacecraft cargo for delivery to the ISS.

V. CubeRRT On-Orbit Operations

A. Overview

CubeRRT's launch to the ISS occurred from the Wallops Flight Facility (WFF) launch pad in Wallops Island, VA at 4:44 AM EDT on May 21st, 2018. The Cygnus cargo craft subsequently docked with the ISS at 8:13 AM EDT on May 24th. CubeRRT was then deployed from the ISS via the Nanoracks CubeSat deployment system on July 13th at 08:35 AM EDT. Payload operations began August 29th, 2018, and occurred as follows:

1) 15:18–15:28 UTC on August 29th, antenna stowed (over ocean, default command state);
2) 22:24–22:34 UTC on September 4th, antenna stowed (over ocean);
3) 13:16–13:26 UTC on September 5th, antenna deployed (over ocean);
4) 15:44–15:54 UTC on September 8th, antenna deployed (ocean to land crossing during which RFE ceased to operate).

Operations after September 8th focused on additional system testing and ultimately operation in an "RDB-only" mode.

CubeRRT's RFE subsystem ceased operations during the data collection on September 8th; datasets after this period show a response consistent with prelaunch testing with the RFE not powered ON. Analyses by the project indicate a failure in the delivery of +7.5 V power to the RFE, although no clear source for this failure has yet to be identified despite extensive on-orbit testing and attempts to restart the RFE. The discussions to follow therefore focus on the three 10-min datasets prior to the cessation of RFE operation, and the more than 5000 h of data collected in the "RDB-only" mode.

B. Datasets With RFE

The first 10-min collect occurred on August 29th in CubeRRT's default command mode with the antenna stowed. Payload telemetry reported during this collect was nominal and showed values similar to those reported in TVAC testing under the cold conditions encountered during this collect. A full sweep over the ten "golden" frequencies with the default 14.4 s dwell on each frequency requires 144 s (or 1440 packets). During the 10-min collect, the sequence repeated four times and continued

into a fifth cycle for which only the first and a partial sweep over the second frequency were obtained. Fig. 10 illustrates results from the measurement by combining multiple 1 GHz reported moment spectra across the ten golden frequencies into a single horizontal axis. Results from the antenna raw moments, the antenna kurtosis, relative variations in antenna over reference load powers, and the onboard generated RFI flags are shown. Note in the default state, compressed spectrum packets are obtained only for two of the twelve antenna measurements per calibration cycle (Fig. 6), and that any ground-based attempt at flag regeneration is impacted by the lack of full spectrum information for each measurement in the cycle. In this case, a full frequency dwell consists of 18 spectrum "packets" each representing a 100 ms integration time. The data on the vertical axis for each frequency is combined over the first four dwells at a given frequency, with each set of 18 moment measurements separated in time by ∼144 s.

The results in upper left plot of Fig. 10 show nominal behaviors in terms of the passband response at each frequency and their time variations. The upper right kurtosis plot confirms that no significant RFI is observed with the exception of the narrow self-generated clock harmonics especially present in the 6.8 GHz frequency (band 1). The lower right plot shows only a modest level of RFI flagging given the absence of RFI; these flags were generated using both the kurtosis and cross-frequency algorithms using the flattened antenna over reference measurements, with the cross-frequency detections subject to the accuracy of the flattening table onboard the spacecraft determined from prelaunch measurements. The increased level of flagging in the 18.7 GHz band (interval 4–5 on the horizontal axis) is also consistent with expectations, as this band overlaps the 19.4 GHz channel for which the Level 2 onboard 4480-point table is optimized. Ground reprocessing confirmed agreement with the onboard generated flags to the level of 1 flag difference out of 128 even in the absence of spectrum moment data for all calibration states, confirming successful onboard RFI detection and flagging operations.

The lower left plot in Fig. 10 shows relative variations in antenna over reference powers generally to be within ±0.05 dB. A larger decrease in power levels in band 1 (6.8 GHz) is observed for the second of the 14.4 s sweeps, after which the power returns to the level observed in the first sweep. These moderate gain variations are consistent with those expected from prelaunch testing.

Measurements during the second collect (22:24–22:34 UTC on September 4th) with the antenna stowed showed similar results and again validated the ability to reproduce the onboard generated flags in ground processing to the expected accuracy. The payload antenna deployment was commanded between the second and third collects, and a third data collection occurred 13:16–13:24 UTC on September 5th. Because the collection occurred over a homogeneous ocean background, no external RFI was expected to be received, and no major changes in raw antenna counts were anticipated (although changes in brightness temperatures were expected following data calibration). A first assessment of the antenna deployment state was conducted by comparing spectra for the "flattened" antenna over reference load datasets pre- and postantenna deployment. Because the flattening tables were developed for the antenna in a deployed
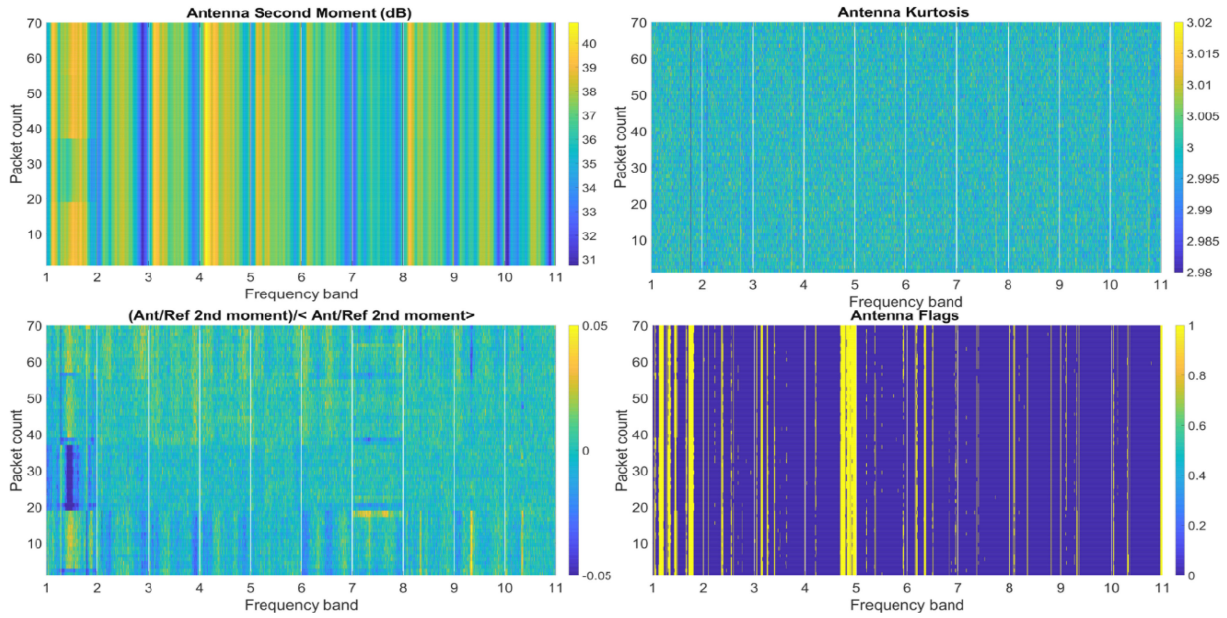
Fig. 10. Results from CubeRRT's ten "golden frequencies" in the first data collect (with the payload antenna stowed) on 8/29: (Upper left) Antenna second moment raw counts in dB. (Upper right) Antenna kurtosis values. (Lower left) Relative variations in dB of antenna over reference load data. (Lower right) On-board generated RFI flags. Note that frequency band 1 occurs in the interval 1–2 on the horizontal axis, band 2 in the interval 2–3, etc.
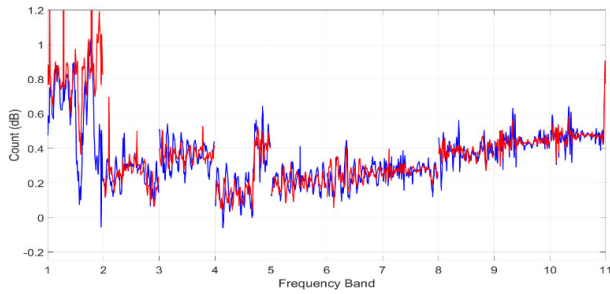

Fig. 11. Antenna over reference load "flattened" data before (blue) and after (red) antenna deployment; the reduced variations in the deployed case confirm successful antenna deployment.

Fig. 12. (Left) CubeRRT A/D capture output with the RFE turned OFF—-only 1–2 bits are varying about the nominal 127 zero value. (Right) Spectrum obtained from left plot showing the presence of the 250 MHz self-generated RFI.

state, the flattened spectra in the deployed state should show a reduced level of variation if the antenna were successfully deployed. Fig. 11 illustrates the resulting spectra, and confirms the expected reduction in passband variations. It is noted however that band 1 shows somewhat larger differences likely due to greater uncertainties in the Level 2 flattening coefficients in this band. The remaining residual variations (at a level typically of <0.1 dB) were to be addressed by continued refinement of the onboard flattening coefficients.

Preliminary calibrations of the over-ocean data obtained on September 5th using prelaunch determined calibration coefficients showed reasonable values for ocean emissions. However, the inability to acquire additional data limited complete determination of the antenna loss correction, so that the accuracy of the calibrated brightness temperatures achieved is uncertain. No obvious RFI was observed during this collection, although some RFI flags were raised due to residual passband variations not fully compensated by the prelaunch Level 2 flattening tables used in the onboard detection process.
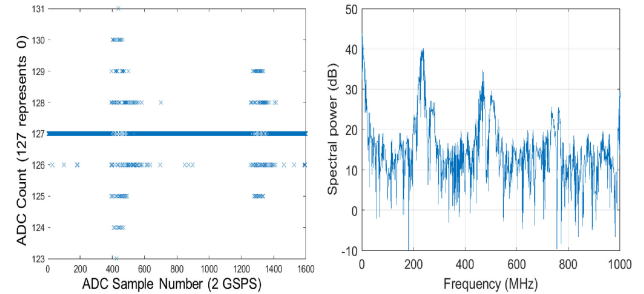
C. RDB-Only Datasets

With the RFE turned OFF, CubeRRT's RDB measures any residual low-level power on its input. This power level is not related to the RF power observed by the antenna and does not vary with the antenna pointing, spacecraft location, or spacecraft attitude. These facts enable CubeRRT to be operated in an "RDB-only" mode in which the spacecraft attitude is selected either to maximize power availability to the spacecraft (i.e., a "sun pointing" mode) or to minimize spacecraft drag. These attitudes as well as the elimination of RFE power consumption allow the payload to be operated at a higher duty cycle. Tests were performed in varying attitude and duty cycle combinations, including 50%, 75%, and 100%, before a final compromise of 75% duty cycle operations in a reduced drag attitude was selected for continued use.

To understand detailed properties of the RDB input signals, multiple A/D "captures" were performed. Fig. 12 illustrates one such capture, in which 1600 digital samples at the 2 GSPS
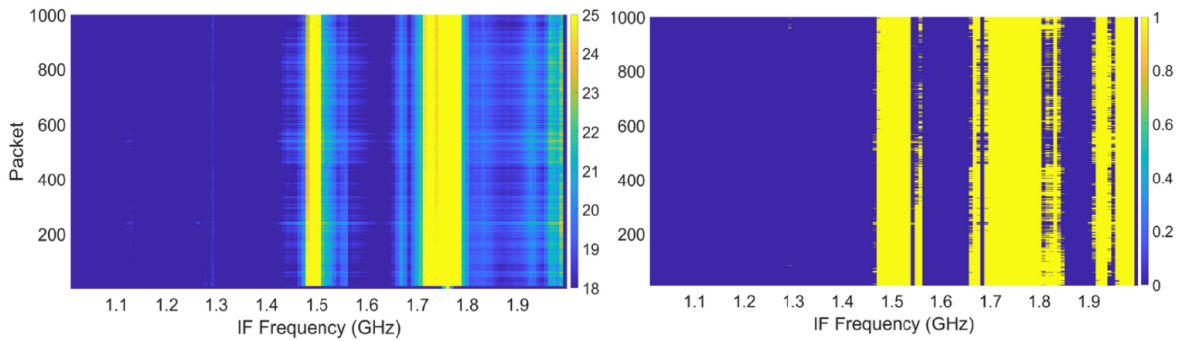
Fig. 13. Example spectra from RDB-only mode (left) and corresponding flags generated by the cross-frequency algorithm with adjusted thresholds and flattening turned OFF (right).

sampling rate are plotted. The vertical axis represents the A/D sampled value, with the value 127 representing a 0 signal. The results show that only 1–2 b of the A/D are varying (i.e., a very low input power level compared to operations with the RFE turned ON). It is still possible to perform a Fourier transform of these samples to examine their spectral content; the right portion of Fig. 12 illustrates this spectrum, and shows that the 250 MHz clock harmonics are still observable, at least partially (note the limited time duration of the A/D capture limits the spectral resolution of the right plot). These "self-RFI" signals therefore still provide an opportunity for demonstrating onboard detection and filtering of RFI.

Given the low power levels obtained in RDB-only mode, adjustments were made to CubeRRT's kurtosis and cross-frequency detection thresholds. In particular, the lower power levels showed increased errors in the computation of the signal kurtosis, and the kurtosis algorithm was "turned OFF" from real-time operation. The cross-frequency algorithm remained available, and was operated without either Level 2 or Level 3 flattening (since there is also no change in calibration state for RDB-only observations) at an increased threshold level. Fig. 13 illustrates an example spectrum obtained in RDB-only mode, along with the corresponding flags generated by the cross-frequency algorithm. The results show the expected detection of the clock harmonic signals, and flag reproduction in ground processing again successfully validates the onboard computations.

Although the "scene" observed in RDB-only mode remains relatively constant in time, the left plot of Fig. 13 does show some apparent variation in signal levels with time that are highly correlated to the RDB reported FPGA temperature. Changes in either the RDB A/D "gain" or in the noise power level itself cause these small variations in time.

RDB-only mode measurements have continued through the time of this writing during periods in which other testing was not conducted, with current measurements continuing at 75% duty cycle. A data management strategy has also been implemented by reporting only the total channel powers, given the extensive RDB-only mode datasets already available for which any anomalous behaviors can be readily detected. This "low data rate" mode of operations also allows the data downlink volume to be managed even with the payload operating at 75% duty cycle. These procedures have allowed CubeRRT to reach ∼5000 h of observation data reported on the ground, without any failure of the RDB's operations.

VI. CONCLUSION

The success of CubeRRT's RDB in operating more than 5000 h on-orbit successfully to date without any evidence of degradation or unexpected interruption represents the primary accomplishment of the CubeRRT mission. The RDB has demonstrated on-board detection and filtering of RFI, so that future radiometer missions can manage this critical challenge without requiring significant increases in data downlink volume. The success of CubeRRT's kurtosis and cross-frequency RFI detection algorithms has also been demonstrated, along with the innovations of CubeRRT's "flattening" approaches to enhance detection sensitivity even in the presence of significant passband response variations. The provision of these processing capabilities in a package of less than 0.25 U volume, 170 g mass, and less than 10 W power consumption further represents a major enabling capability for future radiometer missions. Although the early cessation of RFE operations limited the mission's ability to provide information on the global 6–40 GHz RFI environment and to demonstrate successful processing over a wide range of RFI types, the clear success of the RDB in accomplishing real-time detection and filtering represents a major step forward in addressing the RFI challenge for future microwave radiometer missions.

As of the time of this writing, key potential adopters include the Copernicus Imaging Microwave Radiometer (CIMR) of the European Union, which is currently under consideration for selection as part of the Copernicus Next Generation program [32]. CIMR includes microwave radiometer channels at L, C, X, K, and Ka bands, all of which are known to be impacted by RFI to varying degrees. A processor providing onboard RFI filtering has been proposed [33] and is likely to be a key part of the mission design. CubeRRT's results are available to influence this development and to serve potentially as a candidate design for adoption by the mission.

The increasing interest in the use of frequencies lower than 1 GHz for microwave radiometry [34]–[39] also will motivate the adoption of real-time RFI processing systems. This frequency range provides desirable properties in terms of monitoring ocean and land surfaces as well as the cryosphere, but is heavily impacted by RFI [1]. Real-time digital processing over

a wide bandwidth will be a key technology for realizing the potential of this emerging area.

REFERENCES

[1] M. H. Cohen and A. J. Gasiewski (co-chairs), *Spectrum Management for Science in the 21st Century*. Washington, DC, USA: National Research Council, 2010.

[2] Presidential memorandum: Unleashing the wireless broadband revolution, Jun. 28th, 2010. [Online]. Available: https://obamawhitehouse.archives.gov/the-press-office/presidential-memorandum-unleashing-wireless-broadband-revolution

[3] "Global 5G wireless networks threaten weather forecasts," *Nature*, Apr. 26th, 2019. [Online]. Available: https://www.nature.com/articles/d41586-019-01305-4

[4] "Fifth-generation broadband wireless threatens weather forecasting," *Physics Today*, vol. 72, no. 8, pp. 24–26, Aug. 2019.

[5] M. Younis *et al.*, "Interference from 24-GHz automotive radars to passive microwave Earth remote sensing satellites," *IEEE Trans. Geosc. Rem ote Sens.*, vol. 42, pp. 1387–1398, Jul. 2004.

[6] E. Njoku, P. Ashcroft, T. Chan, and L. Li, "Global survey and statistics of radio frequency interference in AMSR-E land observations," *IEEE Trans. Geosc. Rem ote Sens.*, vol. 43, pp. 938–947, May 2005.

[7] L., Li, P. W. Gaiser, M. H. Bettenhausen, and W. Johnston, "WindSat radio-frequency interference signature and its identification over land and ocean," *IEEE Trans. Geosci. Remote Sens.*, vol. 44, no. 3, pp. 530–539, Mar. 2006.

[8] S. W. Ellingson and J. T. Johnson, "A polarimetric survey of radio frequency interference in C- and X-bands in the continental United States using WindSAT radiometry," *IEEE Trans. Geosc. Remote Sens.*, vol. 44, no. 3, pp. 540–548, Mar. 2006.

[9] E. Daganzo-Eusebio, R. Oliva, Y. H. Kerr, S. Nieto, P. Richaume, and S. M. Mecklenburg, "SMOS radiometer in the 1400–1427-MHz passive band: Impact of the RFI environment and approach to its mitigation and cancellation," *IEEE Trans. Geosci. Remote Sens.*, vol. 51, no. 10, pp. 4999–5007, Oct. 2013.

[10] D. W. Draper, "Radio frequency environment for Earth-observing passive microwave imagers," *IEEE J. Sel. Top ics Appl. Earth Obs erv. Remote Sens.*, vol. 11, no. 6, pp. 1913–1922, Jun. 2018.

[11] S. W. Ellingson, G. A. Hampson, and J. T. Johnson, "Design of an L-band microwave radiometer with active mitigation of interference," in *Proc. IEEE Int. Geosci. Remote Sens. Symp., Conf. Proc.*, 2003, pp. 1751–1753.

[12] C. S. Ruf, S. M. Gross, and S. Misra, "RFI detection and mitigation for microwave radiometry with an agile digital detector," *IEEE Trans. Geosci. Remote Sens.*, vol. 44, no. 3, pp. 694–706, Mar. 2006.

[13] S. Misra, P. N. Mohammed, B. Guner, C. S. Ruf, J. R. Piepmeier, and J. T. Johnson, "Radio frequency interference detection algorithms in microwave radiometry: A comparative study," *IEEE Trans. Geosci. Remote Sens.*, vol. 47, no. 11, pp. 3742–3754, Nov. 2009.

[14] B. Guner, N. Niamsuwan, and J. T. Johnson, "Time and frequency blanking for RFI mitigation in microwave radiometry," *IEEE Trans. Geosci. Remote Sens.*, vol. 45, no. 11, pp. 3672–3679, Nov. 2007.

[15] B. Guner and J. T. Johnson, "Performance study of a cross-frequency detection algorithm for pulsed sinusoidal RFI in microwave radiometry," *IEEE Trans. Geosci. Remote Sens.*, vol. 48, no. 7, pp. 2899–2908, Jul. 2010.

[16] "Radio Frequency Interference: Identification, Mitigation, and Impact Assessment," *Special Issue IEEE Trans. Geosci. Remote Sens.*, Oct. 2013.

[17] D. Entekhabi *et al.*, "The soil moisture active and passive (SMAP) mission," *Proc. IEEE*, vol. 98, no. 5, pp. 704–716, May 2010.

[18] J. R. Piepmeier *et al.*, "Radio frequency interference mitigation for the Soil Moisture Active Passive microwave radiometer," *IEEE Trans. Geosci. Remote Sens.*, vol. 52, no. 1, pp. 761–775, Jan. 2014.

[19] M. Andrews *et al.*, "The ultra-wideband software defined microwave radiometer (UWBRAD): Calibration, RFI processing, and initial campaign results," *IEEE Trans. Geosci. Remote Sens.*, vol. 56, no. 10, pp. 5923–5935, Oct. 2018.

[20] S. Misra *et al.*, "Development of an on-board wide-band processor for RFI detection and filtering," *IEEE Trans. Geosci. Remote Sens.*, vol. 57, no. 6, pp. 3191–3203, Jun. 2019.

[21] J. Lahtinen *et al.*, "Real-time RFI processor for future spaceborne microwave radiometers," *IEEE J. Sel Topics Earth. Observ. Remote Sens.*, vol. 12, no. 6, pp. 1658–1669, Jun. 2019.

[22] J. Johnson *et al.*, "The CubeSat radiometer radio frequency interference technology validation (CubeRRT) mission," in *Proc. Int. Geosci. Remote Sens. Symp.*, 2016, pp. 299–301.

[23] C. Ball *et al.*, "Development of the CubeSat radiometer radio frequency interference technology validation (CubeRRT) system," in *Proc. Int. Geosci. Remote Sens. Symp.*, 2017, pp. 5942–5945.

[24] S. Misra *et al.*, "The CubeSat radiometer radio frequency interference technology validation (CubeRRT) mission: Performance and development of the digital backend technology," in *Proc. Int. Geosci. Remote Sens. Symp.*, 2017, pp. 1251–1254.

[25] S. Misra *et al.*, "CubeSat radiometer radio frequency interference technology validation (CubeRRT) mission: Enabling future resource-constrained science missions," in *Proc. Int. Geosci. Remote Sens. Symp.*, 2018, pp. 6308–6311.

[26] C. McKelvey *et al.*, "Testing and operational planning of the CubeSat radiometer radio frequency interference technology validation (CubeRRT) system," in *Proc. Int. Geosci. Remote Sens. Symp.*, 2018, pp. 297–300.

[27] C. Ball *et al.*, "The CubeSat radiometer radio frequency interference technology validation (CubeRRT) mission," in *Proc. 32nd Ann. AIAA/USU Conf. Small Satellites, Proc.*, 2018.

[28] S. Misra *et al.*, "CubeRRT: First ever demonstration of spaceborne onboard radio frequency interference filtering technology," presented at Int. Geosci. Remote Sens. Symp., Yokohama, Japan, 2019.

[29] J. K. Che *et al.*, "6 GHz to 40 GHz CubeSat radiometer antenna system," *IEEE Trans. Ant. Prop ag.*, vol. 67, no. 5, pp. 3410–3415, May 2019.

[30] CubeSat Design Specification (CDS), Rev 13. [Online]. Available: https://www.cubesat.org/resources

[31] *Poly Picosatellite Orbital Deployer Mk III ICD (P-POD Mk III ICD)*, California Polytech. State Univ., San Luis Obispo, CA, USA.

[32] L. Kilic *et al.*, "Expected performances of the Copernicus imaging microwave radiometer (CIMR) for an All-weather and high spatial resolution estimation of ocean and sea ice parameters," *J. Geophysical Res: Oceans*, vol. 123, pp. 7564–7580, 2018.

[33] S. S. Kristensen *et al.*, "Developments of RFI detection algorithms and their application to future European spaceborne systems," in *Proc. Int. Geosci. Remote Sens. Symp.*, 2019, pp. 4451–4454.

[34] K. Jezek *et al.*, "500–2000 MHz brightness-temperature spectra of the Northwestern Greenland ice sheet," *IEEE Trans. Geosci. Remote Sens.*, vol. 56, no. 3, pp. 1485–1496, Mar. 2018.

[35] K. Jezek *et al.*, "Remote sensing of sea ice thickness and salinity with 0.5-2GHz microwave radiometry," *IEEE Trans Geosci. Rem. Sens.*, vol. 57, no. 11, pp. 8672–8684, Nov. 2019.

[36] N. Ye *et al.*, "Towards multi-frequency soil moisture retrieval using P-and L-band passive microwave sensing technology," in *Proc. IEEE Int. Geosci. Remote Sens. Symp.*, 2018, pp. 3707–3710.

[37] N. Boopathi *et al.*, "Towards soil moisture retrieval using tower-based P-band radiometer observations," in *Proc. IEEE Int. Geosci. Remote Sens. Symp.*, 2018, pp. 1407–1410.

[38] S. Misra *et al.*, "A next generation microwave instrument for cold water salinity measurement," in *Proc. Amer. Geophysical Union, Fall Meeting, Proc.*, 2018.

[39] E., Dinnat *et al.*, "Next generation spaceborne instrument for monitoring ocean salinity with application to the coastal zone and cryosphere," in *Proc. 15th Specialist Meeting Microw. Radiometry Remote Sens. Environ.*, 2018.

Joel T. Johnson (Fellow, IEEE) received the bachelor of electrical engineering degree from the Georgia Institute of Technology, Atlanta, GA, USA, in 1991, and the S.M. and Ph.D. degrees from the Massachusetts Institute of Technology, Cambridge, MA, USA, in 1993 and 1996, respectively.

He is currently the Burn and Sue Lin Endowed Professor with the Department of Electrical and Computer Engineering and ElectroScience Laboratory at The Ohio State University, Columbus, OH, USA. His research interests include microwave remote sensing, propagation, and electromagnetic wave theory.

Dr. Johnson is a member of commissions B and F of the International Union of Radio Science (URSI), and a member of Tau Beta Pi, Beta Kappa Nu, and Phi Kappa Phi. He was a past chair of the GRSS Technical Committee on Frequency Allocations in Remote Sensing (FARS). He served as Technical Program Co-Chair of the 2017 International Geoscience and Remote Sensing Symposium (IGARSS). He was the recipient the 1993 Best Paper Award from the IEEE Geoscience and Remote Sensing Society, the Office of Naval Research Young Investigator Award, the National Science Foundation Career Award, and the Presidential Early Career Award for Scientists and Engineers (PECASE), in 1997, and was recognized by the U. S. National Committee of URSI as a Booker Fellow, in 2002. He served as an Associate Editor for the IEEE TRANSACTIONS ON GEOSCIENCE AND REMOTE SENSING, since 2000.

Christopher Ball (Member, IEEE) received the A.B. degree in physics from Harvard University, Cambridge, MA, USA, in 1992, and the M.S. and Ph.D. degrees from The Ohio State University, Columbus, OH, USA, in 1994 and 1998, respectively.

He has served as a Postdoctoral Researcher with the Harvard-Smithsonian Center for Astrophysics, Cambridge, MA, USA, from 1998 to 2000, where he performed laser spectroscopy measurements of exotic carbon chain and ring compounds in support of optical astronomy applications. Starting in 2000, he joined the Battelle Memorial Institute, Columbus, OH, USA, where he developed sensor technologies and analysis methods for defense, environmental, and industrial applications. In 2016, he joined the ElectroScience Laboratory at The Ohio State University, Columbus, OH, USA, where he continues to perform research and development activities for sensors operating across the electromagnetic spectrum. Recent examples include microwave radiometry for Earth science remote sensing, infrared imaging and spectroscopy for methane detection and food characterization, and millimeter/submillimeter wave spectroscopy for trace gas detection.

Chi-Chih Chen, photograph and biography not available at the time of publication.

Christa McKelvey, photograph and biography not available at the time of publication.

Graeme E. Smith, photograph and biography not available at the time of publication.

Mark Andrews, photograph and biography not available at the time of publication.

Andrew O'Brien received the Ph.D. degree in electrical engineering from The Ohio State University, Columbus, OH, USA, in 2009. He currently is a Research Scientist with the ElectroScience Laboratory at The Ohio State University, Columbus, OH, USA. His primary research focus is remote sensing systems using GNSS reflectometry (GNSS-R). Other research activities include precision GNSS receiver design, antenna arrays, adaptive antenna electronics, RF emitter geolocation, interference mitigation, and radar system signal processing.

J. Landon Garry, photograph and biography not available at the time of publication.

Sidharth Misra (Senior Member, IEEE) received the B.E degree in electronics and communication engineering from Gujarat University, Ahmedabad, Gujarat, India, in 2004, and the M.S. degree in electrical engineering and computer science from the University of Michigan, Ann Arbor, MI, USA, in 2006. He received the Ph.D. degree from the Department of Atmospheric, Oceanic and Space Sciences, University of Michigan, in 2011.

He is currently a Technologist with the NASA Jet Propulsion Laboratory (JPL) in Pasadena, CA, USA. He joined JPL as a member of the Microwave Systems Technology group, in 2011. He was a Research Engineer with the Space Physics Research Laboratory, University of Michigan and a Research Assistant with the Danish National Space Center, Technical University of Denmark (DTU), Lyngby, Denmark. He was also with the Space Applications Center, Indian Space Research Organization, Ahmedabad, India. He was on the calibration team of the Aquarius radiometer, and was the Instrument-Scientist on the RACE mission. He is currently on the science team of Soil Moisture Active Passive (SMAP) and radiometer calibration team member for the Juno microwave radiometer. He is also the Digital Back-End Lead for the CubeRRT mission and Instrument Manager for the Passive and Active L- and S-band (PALS) airborne system. His research interests include radio frequency interference algorithm development and mitigation, microwave radiometer system development and calibration.

Dr. Misra was the recipient of the IGARSS 2006 Symposium Prize Paper Award, the 2009 IEEE-GRSS Mikio Takagi Award, and 2012 IEEE TGRS Best Reviewer Award. He was the recipient of the JPL Charles Elachi Early Career Award, in 2016, the NASA Early Career Public Achievement Medal, in 2017, and the NASA Exceptional Technology Achievement Medal, in 2019. He was also the recipient of six NASA Group Achievement Awards. He is an Associate Editor for the IEEE GEOSCIENCE AND REMOTE SENSING LETTERS.

Rudi Bendig, photograph and biography not available at the time of publication.

Carl Felten, photograph and biography not available at the time of publication.

Shannon Brown, photograph and biography not available at the time of publication.

Robert F. Jarnot, photograph and biography not available at the time of publication.

Jonathon Kocz, photograph and biography not available at the time of publication.

Kevin Horgan, photograph and biography not available at the time of publication.

Jared F. Lucey, photograph and biography not available at the time of publication.

Joseph J. Knuble received the B.S. degree in electrical and computer engineering from Worcester Polytechnic Institute, Worcester, MA, USA, in 2002 and the M.S. degree in Electrical and Computer Engineering from Johns Hopkins University, Baltimore, MD,USA, in 2007.

In 2002, he joined the Microwave Instrument and Technology Branch, at NASA's Goddard Space Flight Center, Greenbelt, MD, USA, where he worked in technology development for microwave remote sensing and spaceflight radiometers. He was the Lead Engineer for the SMAP Radiometer Front End (RFE) electronics. He was the Lead RF Systems Engineer, Project Manager, and Co-Investigator with the Signals of Opportunity Airborne Demonstrator (SoOp-AD) funded through NASA's Earth Science Technology Office (ESTO) 2013 Instrument Incubator Program (IIP). He developed the phase-locked-oscillator (PLO) system for CubeRRT. In 2017, he joined the Instruments and Payload Systems Engineering Branch of Goddard Space Flight Center (GSFC). He currently works with the Plankton, Aerosol, Cloud, Ocean Ecosystem (PACE) Mission Ocean Color Instrument (OCI) as the Lead Instrument Systems Engineer for prelaunch calibration and on-orbit solar calibration.

Mike Solly, photograph and biography not available at the time of publication.

Carlos Durán Avilés was born in Mayagüez, Puerto Rico, in 1983. He received the B.S. degree in electrical engineering from University of Puerto Rico, Mayagüez Campus, Puerto Rico, in 2006.

He is currently working with NASA Goddard Space Flight Center at Greenbelt, MD, USA, working for Code 596 Components and Hardware Branch.

Jinzheng Peng received the B.S. degree in electrical engineering from Wuhan University, Wuhan, China, in 1991, the M.S. degree in electrical and computer engineering from the University of Massachusetts, Amherst, MA, USA, in 2003, and the Ph.D. degree in electrical engineering from the University of Michigan, Ann Arbor, MI, USA, in 2008. From 1991 to 2000, he was with the Beijing Institute of Remote Sensing Equipment, Beijing, China.

He is currently with Goddard Earth Sciences Technology and Research, Universities Space Research Association, Columbia, MD, USA, and with the NASA's Goddard Space Flight Center, Greenbelt, MD, USA. His current research interests include system-level concept design, analysis, calibration/validation, and algorithm development for microwave remote sensing instruments.

Dr. Peng is the recipient of the four NASA group Achievement Awards and two NASA Robert H Goddard Exceptional Achievement awards.

Damon Bradley, photograph and biography not available at the time of publication.

Jeffrey R. Piepmeier, (Senior Member, IEEE) received the B.S. Engineering degree in electrical concentration from LeTourneau University, Longview, Texas, in 1993, and the M.S. and Ph.D. degrees in electrical engineering from the Georgia Institute of Technology, in 1994 and 1999, respectively. He is currently the Chief Passive Microwave Instrument Engineer in the Instrument Systems and Technology Division at NASA's Goddard Space Flight Center and serves as a Deputy Coordinator for the Aerosols, Clouds, Convection and Precipitation architecture study and as Technology Co-Lead for the Planetary Boundary Layer study team. He is Instrument Scientist for the SMAP radiometer and GPM Microwave Imager. Previously at GSFC, he was Associate Head of the Microwave Instruments and Technology Branch and Instrument System Engineer for the Aquarius Radiometer. He was Deputy PI on the IceCube cubesat mission and lead the Goddard teams on the CubeRRT and SNOOPI cubesat missions. Before joining NASA, he was a Student Employee at Vertex Communications Corp. and a Shackleford Fellow with Georgia Tech Research Institute. His research interests include microwave radiometry and technology development to enable the next generation of microwave sensors.

Dr. Piepmeier is a member of IEEE and URSI (Commission F). He is a past Chairperson of the GRSS Instrumentation and Future Technologies technical subcommittee and past chairperson of the National Academies' Committee on Radio Frequencies (CORF). Dr. Piepmeier was recipient of an Excellence in Federal Career Gold Award (Rookie-of-the-year) in 2000, was a 2002 NASA Earth Science New Investigator. He has received five NASA Group Achievement Awards, NASA's Exceptional Engineering Achievement Medal for advances in RFI mitigation technology, NASA's Exception Achievement Medal for significant contributions to the Aquarius/SAC-D mission, and NASA.s Outstanding Leadership Medal for contributions of Aquarius, GPM and SMAP.

Doug Laczkowski, photograph and biography not available at the time of publication.

Matt Pallas, photograph and biography not available at the time of publication.

Nick Monahan, photograph and biography not available at the time of publication.

Ervin Krauss, photograph and biography not available at the time of publication.